Available online at www.sciencedirect.com
ScienceDirect
Journal of Magnetic Resonance 188 (2007) 357–366
JMR Journal of Magnetic Resonance
www.elsevier.com/locate/jmr

3D MRI of non-Gaussian ^{3}He gas diffusion in the rat lung

Richard E. Jacob [a,*], Gernot Laicher [b], Kevin R. Minard [a]

[a] *Pacific Northwest National Laboratory, 902 Battelle Blvd. MS P7-58, Richland, WA 99352, USA*
[b] *University of Utah, Salt Lake City, UT 84112, USA*

Received 7 June 2007; revised 7 August 2007
Available online 24 August 2007

Abstract

In ^{3}He magnetic resonance images of pulmonary air spaces, the confining architecture of the parenchymal tissue results in a non-Gaussian distribution of signal phase that non-exponentially attenuates image intensity as diffusion weighting is increased. Here, two approaches previously used for the analysis of non-Gaussian effects in the lung are compared and related using diffusion-weighted ^{3}He MR images of mechanically ventilated rats. One approach is model-based and was presented by Yablonskiy et al., while the other approach utilizes the second order decay contribution that is predicted from the cumulant expansion theorem. Total lung coverage is achieved using a hybrid 3D pulse sequence that combines conventional phase encoding with sparse radial sampling for efficient gas usage. This enables the acquisition of nine 3D images using a total of only ~1 L of hyperpolarized ^{3}He gas. Diffusion weighting ranges from 0 s/cm^2 to 40 s/cm^2. Results show that the non-Gaussian effects of ^{3}He gas diffusion in healthy rat lungs are directly attributed to the anisotropic geometry of lung microstructure as predicted by the Yablonskiy model, and that quantitative analysis over the entire lung can be reliably repeated in time-course studies of the same animal.

Keywords: Hyperpolarized ^{3}He; 3D projection reconstruction; Lung; MRI; Non-Gaussian diffusion

1. Introduction

Hyperpolarized ^{3}He gas is currently the most sensitive signal source for visualizing pulmonary air spaces with magnetic resonance imaging (MRI) [1–3]. Its high rate of diffusion (i.e., Brownian motion) is also easily measured and is sensitive to the confining effects of lung tissue [4–6]. Approaches for exploiting this to probe lung microstructure utilize pulsed magnetic field gradients that impart additional phase to the signal detected from diffusing molecules [7]. The effect on images acquired using different gradient strengths reflects the influence of airway architecture on the underlying gas dynamics [8–10].

In a free gas where molecular diffusion is unencumbered by surrounding lung tissue, the random nature of Brownian displacements leads to a Gaussian distribution of phases in each resolved volume element [11]. Under these conditions, image intensity decays exponentially with the gas diffusion coefficient D as sensitivity to motion is increased by application of stronger and stronger gradients. By comparison, the effects of gas diffusion in the lung are not as well understood and generally vary depending on employed motion sensitization and local lung structure [12,13]. Results from different studies are therefore often difficult to compare and uncertainty remains concerning available information content.

Historically, sensitivity to molecular diffusion in MRI has been quantified using a so-called b-value, which describes the degree of diffusion weighting. In diffusion-weighted imaging experiments performed with low b-values, the phase accumulated by diffusing molecules is small and the phase distribution is always well approximated by a Gaussian function [14]. Under these conditions, an exponential analysis of measured image decay is rigorously justified. In the lung, this Gaussian approximation has been widely exploited for measuring an apparent diffusion coefficient (ADC) of ^{3}He gas (cf. [15–17]). In lung, the ADC is

* Corresponding author. Fax: +1 509 376 2303.
E-mail address: richard.jacob@pnl.gov (R.E. Jacob).

1090-7807/$ - see front matter © 2007 Elsevier Inc. All rights reserved.
doi:10.1016/j.jmr.2007.08.014

generally much lower than D because pulmonary tissue impedes molecular displacements. In healthy human lung using diffusion times of a few ms, for example, the ADC for ^{3}He is approximately 0.2 cm^2/s—about a factor of four lower than D of freely diffusing ^{3}He in air [6].

Although previous work confirms that the ADC of ^{3}He is sensitive to changes in lung microstructure [8,9,15,18], diffusion-inhibiting structures can result in a substantial deviation from a Gaussian phase distribution. This deviation is manifested through non-exponential signal decay when images are acquired using large b-values [11]. Therefore, additional information than that embodied by the ADC is potentially available for probing lung structure. The study of these non-Gaussian effects, however, is technically challenging since more b-values, and more polarized gas, are generally required to define the non-exponential behavior of the measured signal. Therefore, such studies in conjunction with three-dimensional (3D) imaging of the entire lung require careful gas management and have not yet been reported. Moreover, alternative methods previously employed for analyzing non-Gaussian effects remain to be compared or related. Hence, key questions remain: which analysis methods are most appropriate, under what conditions should they be applied, and how reproducible are derived parameters? In this study each of these outstanding issues is addressed using 3D diffusion-weighted ^{3}He MR images of mechanically ventilated rats. Results are thus relevant to the future utilization of non-Gaussian ^{3}He diffusion as a potential diagnostic tool for probing lung microstructure.

1.1. Theoretical review of non-Gaussian diffusion effects

At low b-values, when the phase accumulated by moving spins is small, the Gaussian approximation is valid and the signal S in diffusion-weighted images exhibits an exponential decay, such that

$$S = S_0 \exp[-bD_{\text{app}}]. \tag{1}$$

Here, S_0 is the signal in an image acquired with no diffusion weighting and D_{app} is the apparent diffusion coefficient (ADC) [7]. For bipolar, diffusion sensitizing gradient pulses, the b-value is defined as:

$$b = \gamma^2 G^2 \delta^2 (\Delta - \delta/3), \tag{2}$$

where γ is the gyromagnetic ratio, G is the strength of the bipolar gradients, δ is the gradient duration, and Δ is the gradient separation [19].

In many biological tissues, the observed signal attenuation measured using higher b-values is not exponential and cannot be accurately fit using Eq. (1). Generally, this is an indication that accumulated spin phase is not Gaussian distributed, or is perhaps characterized by a combination of multiple Gaussian distributions [20,21]. In practice, this situation can arise from the presence of boundaries that restrict diffusion within each resolved volume element (voxel). In an effort to describe non-Gaussian diffusion of ^{3}He gas in the lung, one recent study [22] incorporated the next higher order decay contribution that is predicted from the cumulant expansion theorem. With this approach, the predicted signal decay is described by [21,23]:

$$S = S_0 \exp\left[-bD_{\text{app}} + \frac{K_{\text{app}}}{6}(bD_{\text{app}})^2\right]. \tag{3}$$

Here, K_{app} is termed the apparent diffusional kurtosis (ADK).

In previous work, Trampel et al. [22] measured the ADK *in vivo* in human lungs. Since the ADK is proportional to the fourth moment of molecular displacements, they hypothesized that it should be more sensitive than the ADC to diffusive displacements in structures larger than alveoli, such as bronchiolar airways. By using HP ^{3}He imaging with b-values ranging from 0 to 15 s/cm^2, they showed that Eq. (3) indeed described the signal decay more precisely than Eq. (1). However, the ADK was not related to specific physiological parameters. Herein, we show that the ADK is in fact related to the diffusion anisotropy and that it should therefore be sensitive to changes in tissue organization that affect the anisotropy. In analogous work focusing on water diffusion, Kiselev and Il'yasov [21] performed diffusion-weighted MRI of brain tissue and found the MRI signal decay in gray matter is well described by Eq. (3). They also specified critical values of b below which the approximation in Eq. (3) fits the data well, but above which higher order terms of the cumulant expansion are needed. However, their critical values were expressed in terms of a two-compartment diffusion-model that is commonly employed for brain tissue and is not appropriate in the lung. In this work, we specify conditions for the valid utilization of the kurtosis approach for the analysis of gas diffusion in the lung.

From a practical standpoint, use of the kurtosis approach shown in Eq. (3) is desirable since it assumes no specific model of lung structure, and it is expressed in terms of phenomenological transport coefficients (i.e., D_{app} and K_{app}). In practice this affords flexible application. However, the precise meaning of measured coefficients and their relationship to underlying lung microstructure remains unclear. By comparison, a model-based approach for describing non-Gaussian diffusion effects in lung tissue has been developed by Yablonskiy et al. [24]. This is based on a simplified picture of the lung microstructure at the alveolar and bronchiolar level. The model is based on the assumption that a large number of randomly distributed cylindrical airways are included in each image voxel, with each bronchiole jacketed by open, spherical alveoli. This physical description is well supported by histological images of healthy rat lung tissue (cf. Fig. 1 of Ref [25]).

The Yablonskiy model [24] predicts that the diffusion attenuated signal decay in the deep lung is given by:

$$S = S_0 \exp(-b\overline{D})\left(\frac{\pi}{4bD_{\mathrm{AN}}}\right)^{1/2} \exp\left(\frac{bD_{\mathrm{AN}}}{3}\right)\Phi\left(\sqrt{bD_{\mathrm{AN}}}\right), \tag{4}$$

where $\Phi(x)$ is the error function, $\overline{D}$ is the mean ADC, and D_{AN} is the anisotropy of the ADC. $\overline{D}$ and D_{AN} are related to D_L, the ADC in the longitudinal direction (i.e., along a small airway), and D_T, the apparent diffusion transverse to the airway by:

$$\overline{D} = \frac{1}{3}D_L + \frac{2}{3}D_T, \quad D_{\mathrm{AN}} = D_L - D_T. \tag{5}$$

In their work, Yablonskiy et al. acquired *in vivo* data using six b-values in the range of 0–7.5 s/cm^2 in both normal and emphysematous volunteers. They showed that D_L and D_T are sensitive to emphysematous changes in lung structure. They were also able to relate the mean airway radius R to the transverse diffusivity D_T by incorporating the diffusion propagator solution to the diffusion equation within a two-dimensional circle of radius R. The result gave D_T as a function of the mean airway radius R, the free ^{3}He diffusivity D_0, and the timing parameters of the diffusion weighting gradients (see Equation (8) of Ref. [24]). For this calculation, it was assumed that the phase distribution is Gaussian and that the alveolar walls are impenetrable. Yablonskiy et al. emphasized that the relationship between D_T and R is only an approximation, and that R should be considered as an apparent airway radius, particularly in circumstances of tissue destruction such as in emphysema. However, their calculations of R using this model were in good agreement with histological data. We note that the Yablonskiy model breaks down for situations of isotropic diffusion, such as in large airways or with small voxel sizes.

To facilitate a direct comparison of the kurtosis description and the model-based approach of Yablonskiy et al., we now relate Eq. (3) with Eq. (4). This requires an expansion of the error function in Eq. (4), which gives:

$$\ln\frac{S}{S_0} = -b\left(\overline{D} - \frac{D_{\mathrm{AN}}}{3}\right) + \ln\left(1 - \frac{bD_{\mathrm{AN}}}{3} + \frac{b^2D_{\mathrm{AN}}^2}{10} - \cdots\right). \tag{6}$$

By retaining the first three terms of the error function expansion and by expanding the natural logarithm on the right hand side of Eq. (6), the result is:

$$\ln\frac{S}{S_0} \approx -b\overline{D} + \frac{2}{45}b^2D_{\mathrm{AN}}^2. \tag{7}$$

Direct comparison of Eq. (7) with the kurtosis description in Eq. (3) reveals that $\overline{D}$ is equivalent to D_{app} and:

$$K_{\mathrm{app}} = \frac{4}{15}\frac{D_{\mathrm{AN}}^2}{\overline{D}^2}. \tag{8}$$

By relating K_{app} to physiologically relevant parameters through Eqs. (8) and (5), it achieves practical meaning when applied to the lung. Indeed, because K_{app} is proportional to the square of the diffusion anisotropy, it should be particularly sensitive to changes in the lung structures that contribute to the anisotropy. In regions of the lung where the diffusion anisotropy is small (i.e., when $D_L \approx D_T$), such as in large airways, K_{app} vanishes and the signal decay becomes Gaussian. On the other hand, in the deep lung where D_{AN} is generally larger than $\overline{D}$, $K_{\mathrm{app}} > 0$ indicating non-Gaussian diffusion effects. We note that Eq. (4) also reflects Gaussian diffusion in the limit of $D_{\mathrm{AN}} \to 0$. An alternative derivation of Eq. (8) is presented in the appendix.

Conditions for the valid application of the kurtosis approach can now be defined in terms of a critical b-value b_c, or an approximate limit beyond which the kurtosis approach and the Yablonskiy model no longer agree. The expansion of the error function $\Phi(x)$ in Eq. (6) is accurate to within 3% up to $x \approx 1$ when the first three terms are retained. Therefore, from this approximation we have $b_cD_{\mathrm{AN}} \approx 1$, or:

$$b_c \approx \frac{1}{D_{\mathrm{AN}}}. \tag{9}$$

The value of D_{AN} measured by Yablonskiy et al. in healthy human lung was $\approx$0.3 cm^2/s [24], resulting in $b_c \approx 3.3$ s/cm^2. This is similar to the value of D_{AN} found in rats in this study. To verify the critical b-value in Eq. (9), an artificial data set was generated from Eq. (4) in a b-value range up to 40 s/cm^2 in steps of 0.01 s/cm^2 and with assumed values of D_{AN} and $\overline{D}$. Fig. 1 shows the results of a least squares fit of Eq. (3) to the data over various ranges of b-values. When data with b-values only up to $\approx 1/D_{\mathrm{AN}}$ are included (i.e. Fit 1 of Fig. 1), the fit to Eq. (3) yields values for D_{app} and K_{app} which, together with Eqs. (5) and (8), nearly reproduce the originally assumed values for D_{AN} and $\overline{D}$; see Table 1. As data from larger ranges of b-values are included, the parameters resulting from fits to Eq. (3) deviate increasingly from the original values, indicating

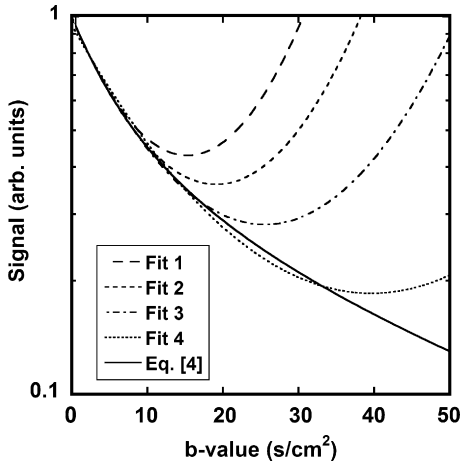

Fig. 1. Test data were generated using the Yablonskiy model (Eq. (4), solid line) and assumed values of $\overline{D}$ and D_{AN}. The data were then fit to the kurtosis equation (Eq. (3)) over various b-value intervals. Fit 1 corresponds to the interval 0–3 s/cm^2; Fit 2 to 0–10 s/cm^2; Fit3 to 0–20 s/cm^2; and Fit 4 to 0–40 s/cm^2. The critical b-value for these test data is $b_c \approx$ 3.3 s/cm^2. Results of the different fits are compared in Table 1.

Table 1
Results from fitting the kurtosis approach (Eq. (3)) to test data that were synthesized using the Yablonskiy model (Eq. (4)) and the assumed values of $\overline{D}$ and D_{AN}, which were typical of rat imaging results in this study

b-range (s/cm^2)	$\overline{D}$ (cm^2/s	D_{AN} (cm^2/s)	D_L (cm^2/s)	D_T (cm^2/s)	K
	0.111[a]	0.299[a]	0.310[b]	0.011[b]	1.935[c]
0–3	0.111	0.285	0.301	0.016	1.774
0–10	0.107	0.251	0.274	0.023	1.472
0–20	0.098	0.208	0.237	0.029	1.198
0–40	0.082	0.159	0.188	0.030	0.918

The critical b-value for this case was $b_c \approx 3.3$ s/cm^2. For the different b-value ranges, the parameters $\overline{D}$ and K were extracted from a fit of Eq. (3), and D_{AN}, D_L, and D_T were calculated using Eqs. (5) and (8). Fit uncertainties were small, generally in the third or fourth decimal place.
[a] Assumed value.
[b] Calculated from Eq. (5) using the assumed values of $\overline{D}$ and D_{AN}.
[c] Calculated from Eq. (8) using the assumed values of $\overline{D}$ and D_{AN}.

that the results are not physically meaningful beyond $b = b_c$. In particular, D_{AN} deviates readily from its true value. The obtained $\overline{D}$, on the other hand, is not as sensitive to higher b-values, but it still deviates in a systematic manner that underestimates its true value. We note that Eq. (3) is not a continually decreasing function of b, as shown in Fig. 1, and gives non-physical results for values of b beyond those included in the fit.

To best describe the non-Gaussian nature of the signal decay of ^{3}He gas in the deep lung, a large range of b-values is necessary. Although the kurtosis approach in Eq. (3) and the Yablonskiy model in Eq. (4) can both be used to describe non-Gaussian diffusion, only Eq. (4) can be applied when b exceeds b_c. Furthermore, Eq. (4) has the advantage of being based on a physiological model. Therefore, we have focused on applying the Yablonskiy model to ^{3}He gas diffusion data acquired in the rat lung.

2. Methods

2.1. Hyperpolarized gas generation and delivery

A home-built polarizer, similar to those described elsewhere [26], but with dual, spectrally narrowed 60 W diode-array lasers [27], was used to generate hyperpolarized (HP) ^{3}He gas via spin-exchange optical pumping [28]. Up to two ≈0.8 L boluses of ^{3}He gas could be polarized simultaneously to a polarization of ≈50% in 10–15 h.

Prior to delivering ^{3}He to the rat, a single bolus of gas was released into a 2 L Tedlar bag (Jensen Inert Products, Coral Springs, FL) that resided in an acrylic box in the imaging magnet's fringe field. The T_1 of the ^{3}He in the bag was measured to be ≈38 min. The ^{3}He was mixed with ≈0.4 L of nitrogen to ensure a sufficient gas volume for an entire nine b-value 3D data acquisition, including 2D setup imaging. The mixture was delivered to the rat by a ventilator (see below) via a positive pressure of nitrogen gas delivered to the box. Relaxation of the ^{3}He due to the oxygen in the lungs was ignored because the imaging time was much shorter than the oxygen-induced T_1 of the ^{3}He [29,30].

2.2. Animal preparation

Male Sprague–Dawley rats (Charles River Laboratories, Wilmington, MA) weighing 200–370 g were used. The broad range in weights is reflective of time-course studies in which the same rats were imaged repeatedly over a period of weeks. Humane animal handling protocols approved by the Institutional Animal Care and Use Committee at Pacific Northwest National Laboratory were followed. The rats were anesthetized with isoflurane anesthetic (typically 3–4% concentration in air), then orally intubated with a 14 gauge catheter tube. To help facilitate insertion of the tracheal tube by reducing oral secretions, a subcutaneous injection of 0.02 ml/kg of glycopyrrolate was administered prior to anesthetization. After the tracheal tube was inserted, the animal was attached supine to the mouthpiece of the ventilator. Usually within 1–2 min the rats were breathing in sync with the ventilator without struggling to breathe at their own rate. Finally, ECG leads were attached to the forearms and a rectal temperature probe was inserted.

Ventilation was accomplished using a home-built, computer controlled, small-animal ventilator based on the designs of Hedlund et al. [31] and Dugas et al [16]. A breathing rate of 50 breaths per minute was sufficient to maintain the rats under gas anesthesia while allowing adequate time for the necessary breathing maneuvers and imaging. For each breathing cycle, ≈1 ml of the ^{3}He/N_2 gas mixture was delivered up to a pressure of ≈5 cm H_2O over 180 ms. As this volume was insufficient to fill the lung, it was followed by ≈4 ml of air delivered to a pressure of ≈15 cm H_2O over 240 ms. This large breath, although much smaller than total lung capacity [32], provided sufficient oxygen for the animal and was allowed to mix thoroughly with the ^{3}He and to evenly distribute deep into the lung. The rat then fully exhaled for 420 ms, after which all ventilator valves were closed. Following a 60 ms delay, data were acquired during a 300 ms breath hold. Data were acquired at full exhalation to assure that the same breath hold level was reliably repeated within each experiment and from rat to rat.

To facilitate animal positioning the rat was secured to a wooden tray along with an NMR-compatible ECG/temperature monitoring unit (SA Instruments Inc., Stony Brook, NY, Model 1025). The tray was then slid into the rf coil on a mating rail. Warm air, typically 50–60 °C, was circulated inside the magnet bore to maintain body temperature. The EGC and temperature data were fed via fiber optic to a laptop PC for monitoring. The rectal temperature was maintained at 35 ± 2 °C, and the pulse rate was typically in the range of 250–330 beats per minute; this varied from rat to rat depending on factors such as body weight, body temperature, and depth of anesthesia.

2.3. Imaging

All images were acquired using a Varian UnityPlus spectrometer (Palo Alto, CA) and a 2.0 T horizontal-bore magnet (Oxford, UK) equipped with self-shielded 150 mT/m gradients (Resonance Research Inc., Billerica, MA) characterized by ≈60 μs rise times. The ventilator provided a trigger signal to the scanner to assure data were acquired during breath hold. Cardiac motion was ignored. A home-built, four-leg birdcage coil was double tuned to ^{1}H and ^{3}He frequencies (84.9 MHz and 64.4 MHz, respectively) [33]. The coil was 15 cm long and 7 cm in diameter, easily accommodating the rat, the ventilator lines, and the ECG/temperature monitoring apparatus. For animal positioning, sagittal proton images were acquired using a standard, multi-slice spin echo sequence.

Various radial sampling strategies have been used by others for 3D ^{3}He spin-density and 2D ADC imaging [4,15,34]. Here, images were acquired using undersampled 3D gradient-echo, radial-projection imaging combined with conventional phase encoding in a "hybrid" imaging scheme (referred to as ZIPR in [35]). Image resolution is generally not severely affected by radial undersampling [34,35]. For example, Peters et al. [35] showed that images from an undersampled projection reconstruction (PR) acquisition incorporating 512 readout points and 128 projections (undersampled in the angular dimension by a factor of 6.3) are comparable to those from a standard FT acquisition of 512 points and 512 phase encodings, while requiring only one fourth the acquisition time. Here, images were radially undersampled by a factor of 1.8. We found experimentally that this undersampling factor optimized spatial resolution and reduced artifacts while facilitating efficient use of the ^{3}He gas. The hybrid sequence included bipolar diffusion-sensitizing gradient pulses along the phase-encode axis; see Fig. 2. Data were acquired radially in the $k_x - k_y$ plane with conventional phase encoding in k_z. Essentially, k-space coverage can be imagined as a stack of bicycle wheels with the spokes aligned from one wheel to the next. Each wheel corresponds to a different $k_x - k_y$ plane, and the spokes correspond to different radial projections. We found that the hybrid imaging was easily implemented using the Varian interface and provided many of the recognized benefits associated with conventional 3D radial acquisition, including time savings from utilizing undersampled radial acquisition [35], the reduction of diffusion losses (by using short gradient echo times in conjunction with highly asymmetric echo sampling) [4], and the over sampling of the center of k-space to reduce motion artifacts [36]. We estimate that, in the deep lung of the rat, the imaging gradients in the read-out direction resulted in diffusion losses of <3% with the asymmetric echo versus >20% had a symmetric echo been used.

To acquire a nine b-value 3D data set, 110 radial projections with 128 complex points per projection and 32 phase encode (PE) steps were employed. Since 32 phase-encoded

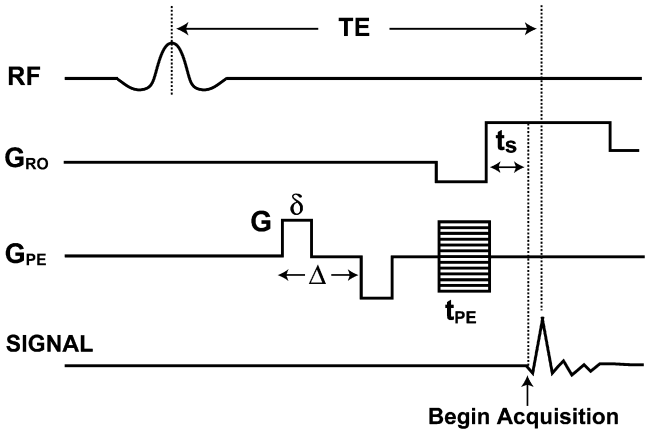

Fig. 2. A schematic of the pulse sequence used for the 3D data acquisition. In this "hybrid" sequence, radial projections in the read-out direction ($k_x - k_y$ plane) were combined with phase encoding along k_z. The echo time TE was 3.85 ms and the phase encoding time t_{PE} was 300 μs. The diffusion sensitizing gradient strength G and timing parameters δ and Δ are defined in the text. A "spoiler" delay t_s of 500 μs was included to allow the gradients to fully stabilize prior to data acquisition. A highly asymmetric echo was acquired, and data points preceding the echo peak were discarded prior to regridding to a 3D Cartesian coordinate system.

projections were acquired per breath, data collection required a total of 990 breathing cycles (with no signal averaging). The hybrid pulse sequence utilized a 500 μs hard rf pulse, with TR = 8 ms, TE = 3.85 ms, and an acquisition bandwidth of 51 kHz. All data were acquired using a constant flip angle, typically 10–12°. To eliminate T_1 effects, the acquisition was interleaved such that a single line of phase-encoded projections (spokes) was acquired for each b-value before proceeding to the next series of spokes. The diffusion weighting gradient pulse width δ was 600 μs, and the gradient pulse separation Δ was 1.8 ms; these parameters remained constant throughout the experiment. The gradient strengths ranged from 0 mT/m to 129.3 mT/m, and these gradients were applied only along the PE axis (i.e., along the z-axis). The b-values used were (in units of s/cm^2): 0, 1, 3, 6, 10, 15, 20, 30, and 40. The gradient levels were calculated from the b-values using Eq. (2); a <1% correction to the gradient values due to their trapezoidal shape was ignored. The phase-encoding gradient did not have a crucial influence on the b-values because this gradient is zero at the center of k-space. The receiver gain, which was calibrated using a water phantom, was increased as the b-value was increased to make use of the full dynamic range of the analog-to-digital converter, and the image signal intensity was then corrected in image processing using the gain calibration. The data were acquired over an FOV of 6.4 cm in the radial direction and 6.4 cm in the phase encoding direction. Imaging time for the full, nine b-value 3D data set was 19.8 min.

2.4. Image reconstruction and processing

Raw 3D ^{3}He data acquired with the hybrid sequence were regridded to a $128 \times 128 \times 32$ 3D Cartesian system

and then Fourier transformed. First, the ^{3}He data were examined for consistent phasing of the various gradient echoes in the $k_z = 0$ "wheel". We found that slight phase variations, presumably caused by eddy currents, can lead to signal reduction at the center of k-space when these complex radial data sets are regridded to a 3D Cartesian system. A small increase in signal-to-noise ratio (S/N) was observed by applying a radial-view dependent phase correction to assure that all gradient echoes had the same phase at the echo peak. The $k_z \neq 0$ wheels were then assumed to need the same phase corrections along each spoke. After this small phase correction, each wheel was processed by performing a density compensation (i.e., multiplication of the raw data with the magnitude of the radial k-vector), convoluting the radial data with a two-dimensional Kaiser-Bessel window function [37], and sampling the result onto a 2D Cartesian grid [38]. Next, the regridded 2D data sets of all the wheels were combined into a 3D Cartesian data set from which the images were reconstructed by a standard 3D Fourier transform. The final image was then deconvoluted by division of the various x–y image planes with the Fourier transform of the two-dimensional Kaiser-Bessel window function [38].

Values of $\overline{D}$ and D_{AN} were calculated on a pixel-by-pixel basis from reconstructed magnitude images by applying a least-squares fit to Eq. (4) using the NonLinearRegress function of Mathematica (Wolfram Research, Champaign, Il). A threshold mask based on the S/N of the unweighted ($b = 0$ s/cm^2) image was applied to eliminate background noise from the resulting diffusion maps. Pixels with a standard error exceeding 50% for $\overline{D}$ and D_{AN} were discarded.

3. Results

A representative 2 mm slice from a 200 g rat for each of the nine different b-values is shown in Fig. 3A. The signal decay with increasing b-value is evident. Fig. 3B shows an enlargement of the last slice, $b = 40$ s/cm^2, with the image brightness increased to show noise. The average S/N in Fig. 3B was ≈9.6, and the average S/N in the $b = 0$ s/cm^2 image was ≈45. These images, as well as the others described below, were cropped from 128×128 pixels to 64×64 pixels after reconstruction to show detail; planar resolution is 0.5 mm × 0.5 mm.

Signal intensity was measured in a region of interest that included most of the right lung, excluding major airways and vasculature, using the slice shown in Fig. 3. Fig. 4 shows the average signal intensity plotted against the b-value. The solid line is a fit of all nine data points to the Yablonskiy model (Eq. (4)), while the dashed line is a fit to the kurtosis expression (Eq. (3)). The dotted line is a fit to Eq. (1) using only the first 4 data points, mimicking acquisition of only a few low b-values. The noise was taken as the mean value of the background of the $b = 40$ s/cm^2 image. The noise floor was incorporated into the fits by the standard root-sum-squares method [23,39]. As shown in Fig. 4, the Yablonskiy model accurately describes the signal decay, notably including the b-value range of $b > b_c$.

Fig. 5 shows an example of the $\overline{D}$ images for the entire 3D image set of the 200 g rat. Of the 32 slices acquired, 14 contained ^{3}He signal from the lung; the central 12 slices are shown in Fig. 5. The major airways are generally visible as regions of higher $\overline{D}$ values.

Fig. 6 shows images of the calculated values of $\overline{D}$, D_{AN}, D_L, D_T, and mean airway radius R for the single represen-

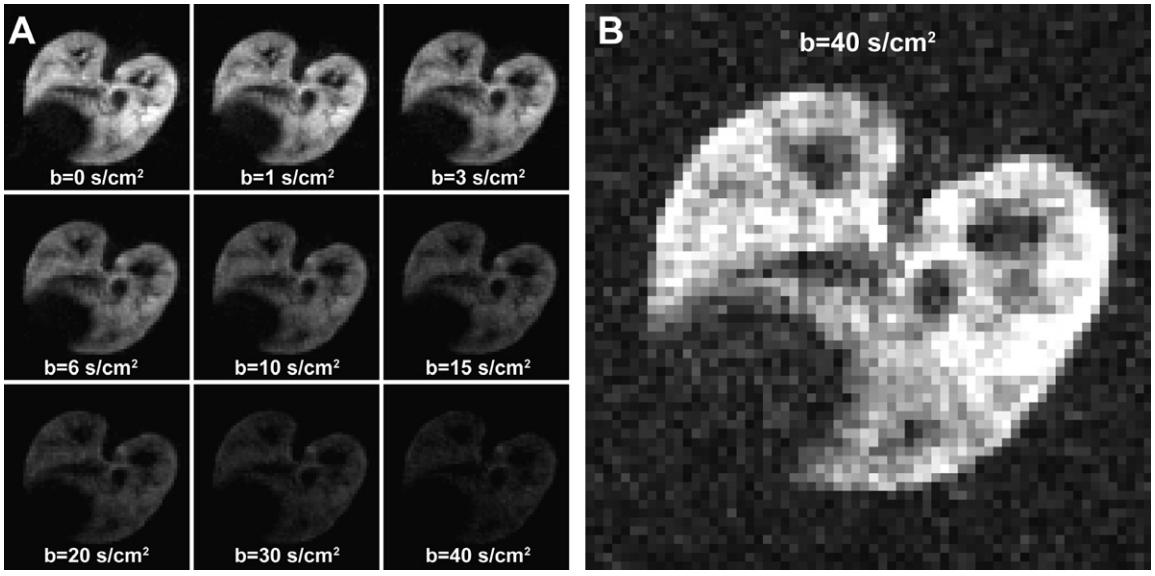

Fig. 3. Representative ^{3}He spin-density images with diffusion weighting of a 200 g rat. (A) ^{3}He signal decay is shown at each of the 9 b-values. The b-values used were (in units of s/cm^2): 0, 1, 3, 6, 10, 15, 20, 30, and 40. (B) An enlarged view of the b = 40 s/cm^2 image with the brightness enhanced to show noise. The images were cropped from 128×128 pixels to 64×64 pixels to show detail. Planar image resolution is 0.5 mm × 0.5 mm, and the slice thickness is 2 mm.

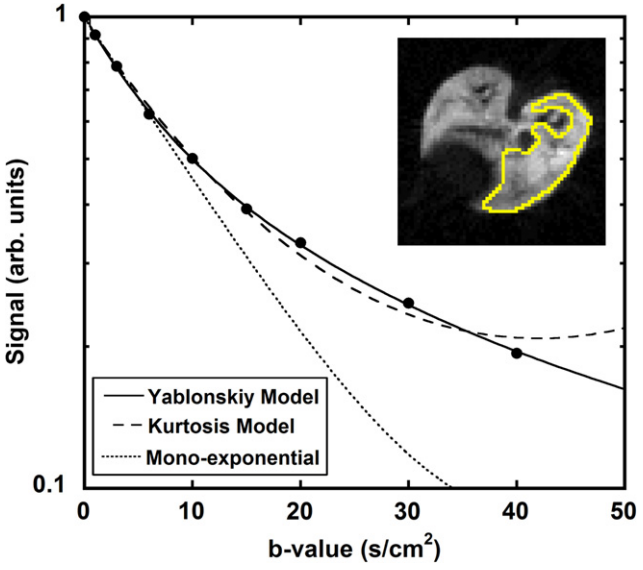

Fig. 4. Using the same image slice shown in Fig. 3A, ^{3}He MRI signal intensity was measured for each of the 9 *b*-values in a region of interest in the right lung. The inset shows the region of interest used. The signal vs. *b*-value is plotted, with the solid line a fit to the Yablonskiy model (Eq. (4)), the dashed line a fit to the kurtosis equation (Eq. (3)), and the dotted line a fit of the first four data points to a mono-exponential (Eq. (1)), imitating the acquisition of only a few low *b*-values. The image noise floor was incorporated into the fits.

tative slice in Fig. 3. $\overline{D}$ and D_{AN} were generated from a fit of the data on a pixel-by-pixel basis to Eq. (4), and D_L and D_T were calculated from Eq. (5). The airway radius R is defined by Yablonskiy et al. as the bronchiole radius plus the approximate alveolar diameter, and was calculated using Eq. (8) in Ref. [24]. Histological measurements of rat airways show an average terminal bronchiole diameter of 0.2 mm and alveolar diameters of 0.05–0.08 mm [32], resulting in $R = 0.15$–0.18 mm. The mean airway radius calculated over the entire lung in our rats (excluding major airways) was 0.16 ± 0.03 mm.

To examine repeatability of the 3D diffusion measurements, a healthy rat was imaged three times with a one week separation between each imaging session. The rat weighed 188 g, 261 g, and 300 g at the three time points. Histograms of $\overline{D}$, including data from the entire lung at each of the time points, are shown in Fig. 7. Although data from Week 1 was found to vary from both Week 2 and Week 3 ($p < 0.05$), there was no significant difference between Week 2 and Week 3 ($p = 0.33$). Similar results were found for D_{AN}. In the range of $0\ \mathrm{cm^2/s} \leqslant \overline{D} \leqslant 0.2\ \mathrm{cm^2/s}$ (i.e. generally excluding larger airways), the mean $\pm$ standard deviation for Week 1, Week 2, and Week 3 were (in units of cm^2/s) 0.098 ± 0.032, 0.091 ± 0.027, and 0.093 ± 0.028, respectively.

4. Discussion

Although both descriptions of non-Gaussian diffusion discussed herein may be useful in different contexts, we have illustrated that the Yablonskiy model [24], described by Eq. (4), portrays the signal decay of ^{3}He gas in rat lungs

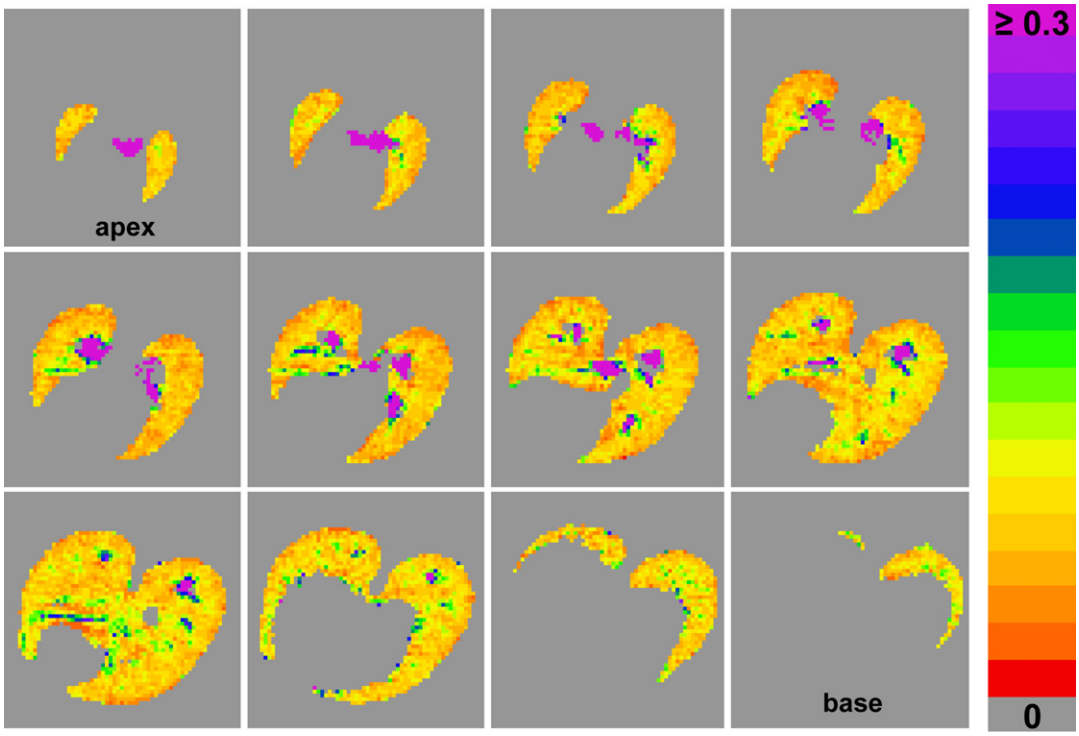

Fig. 5. These images of the average diffusivity $\overline{D}$ in a healthy 200 g rat (same as that shown in Fig. 3) were calculated on a pixel-by-pixel basis from a full 3D ^{3}He data set using the Yablonskiy model (Eq. (4)). Planar resolution is 0.5 mm × 0.5 mm and the slices are 2 mm thick. The color scale is in units of cm^2/s.

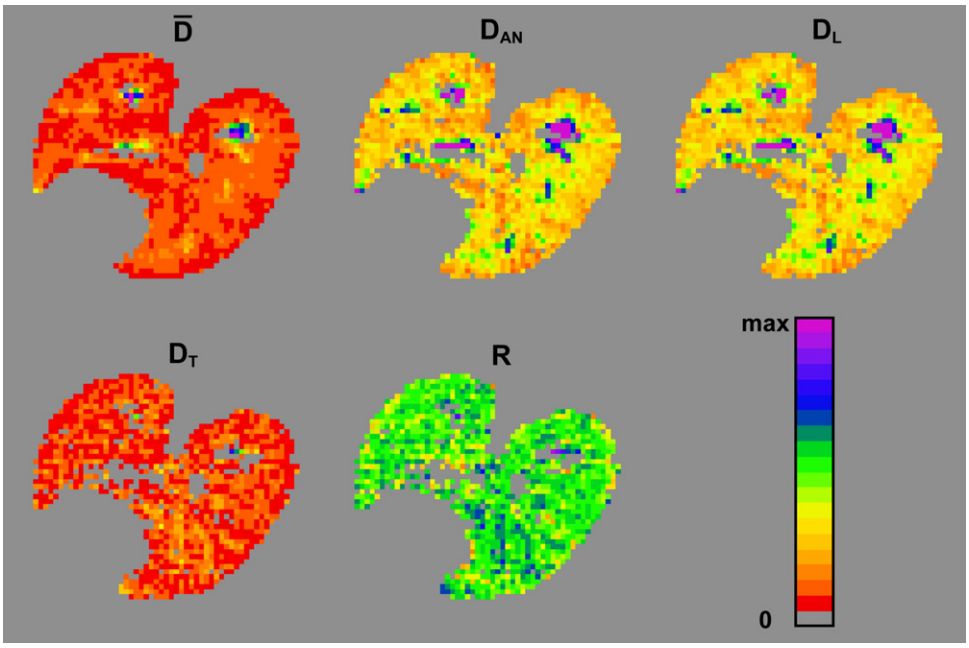

Fig. 6. A single representative slice (same as that shown in Fig. 3) showing maps of $\overline{D}$ and D_{AN} calculated from Eq. (4); pixels in which the standard error exceeded 50% were discarded. Maps of D_L and D_T were calculated from Eq. (5), and the mean airway radius R was calculated from Eq. (8) in Ref. [24]. For $\overline{D}$, D_{AN}, and D_L, the color scale max = 0.8 cm^2/s; for D_T, max = 0.04 cm^2/s; for R, max = 0.3 mm. The median values for each of the parameters over the entire lung are: $\overline{D} = 0.087$ cm^2/s, $D_{AN} = 0.24$ cm^2/s, $D_L = 0.25$ cm^2/s, $D_T = 0.0086$ cm^2/s, and $R = 0.16$ mm.

over a wide range of b-values; see Fig. 4. By comparison, the kurtosis approach (Eq. (3)) is not applicable when the critical b-value b_c is exceeded, as shown by Eq. (9) and in Table 1. Moreover, for sufficiently small b-values (i.e., below b_c), the non-exponential behavior of the signal decay is not well defined, bringing into question the quality of diffusional kurtosis measurements when random noise is added to the data. Indeed, when a noise level of 1% is added to the artificial data of Fig. 1 and when 6 evenly spaced b-values are included in the range of 0–b_c (6 b-values were used in [22,24], although b_c was greatly exceeded in [22]), a fit to Eq. (3) results in an uncertainty in D_{app} of only about 5% but an uncertainty in K_{app} of >40%. This serves to emphasize the usefulness of a large range of b-values including $b \gg b_c$, which can only be analyzed reliably with the Yablonskiy model. We note that most modern clinical MRI scanners are capable of achieving b-values well beyond $b_c = 3.3$ s/cm^2. In addition, the Yablonskiy model provides an avenue for estimating the mean airway radius in each voxel, thus potentially opening a direct correlation of MR diffusion measurements with histology, in which airway radius is readily calculated.

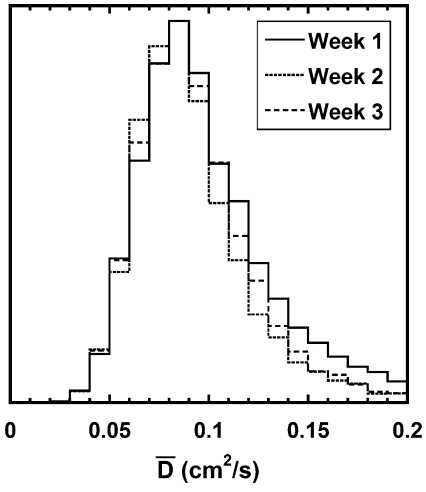

Fig. 7. These three histograms of $\overline{D}$ calculated from the Yablonskiy model (Eq. (4)) include data from the entire lung of a healthy rat imaged with ^{3}He at three time points separated by one week. The histograms have been normalized to the same height and have been truncated at $\overline{D} = 0.2$ cm^2/s to show detail.

Trampel et al. [22] state that the kurtosis approach was developed for the purpose of describing "long range" diffusion, in spite of employing a diffusion time of only 1.28 ms. However, we note that the kurtosis equation (Eq. (3)) is model-free with no rigorous assumptions regarding diffusion times or length scales. Indeed, Eq. (8) shows that the kurtosis is proportional to D_{AN}^2 and thus is a measure of how D_T differs from D_L within an alveoli-lined bronchiole. We emphasize that, as shown in Eq. (9), the validity of the kurtosis approach, inasmuch as physiologically relevant parameters are obtained, depends only on the range of b-values employed. Future studies may illuminate differences between the Yablonskiy model and the kurtosis approach over long diffusion time scales (i.e., seconds or hundreds of milliseconds).

The application of Eq. (4) to the 9 b-value, 3D images acquired in the healthy rats resulted in the highly homogeneous diffusion maps shown in Figs. 5 and 6. Such homo-

geneity in diffusion maps of healthy lungs is typical (cf. [6,9,40]). In addition, Fig. 7 shows that the diffusion measurements are repeatable in the same rat at different times. These results suggest that both the 3D hybrid imaging and the Yablonskiy model can be applied to reliably assess specific aspects of lung microstructure over the entire lung in comparative studies and time-course experiments.

We have demonstrated a technique for acquiring multi-*b*-value 3D data sets for ^{3}He gas diffusion measurements in rat lungs *in vivo*. Importantly, we have shown that a time-efficient 3D pulse sequence can generate images of sufficient quality and resolution for localized calculation of the mean diffusivity $\overline{D}$ and the diffusion anisotropy D_{AN}. This was achieved by implementing a combination of undersampled radial projection imaging and conventional phase encoding. The undersampling allowed for sufficient time savings to acquire nine full 3D data sets using a single bolus ($\sim$1 L) of HP ^{3}He gas. Conversely, to fully satisfy the Nyquist criterion for radial sampling in this experiment, 200 projections would be required [35], stretching the data acquisition to 36 min and consuming $\approx$2 L of the ^{3}He gas mixture.

In practice, undersampled PR imaging may result in radial streaking artifacts, as opposed to aliasing artifacts common in undersampled FT imaging. These artifacts can be minimized by choosing a FOV larger than the object size, since the radial projections will be more closely spaced over the sample than they are at the edges of the FOV. The number of radial projections required to satisfy the Nyquist criterion is given by [41]:

$$N_P = \pi \frac{d}{\mathrm{FOV}} N_R, \tag{10}$$

where N_P is the number of projections, N_R is the number of radial points, and d is the diameter of the object. In this study, we regridded the data to a FOV of 6.4 cm $\times$ 6.4 cm, approximately 2$\times$ the linear dimension of an axial lung slice. The number of radial points retained to generate a 128×128 image was less than the number of acquired points. For example, in order to fill the 128×128 Cartesian grid for each $k_x - k_y$ plane, 64 radial points (of the 128 acquired along each projection) were retained along the k_x or k_y axis while $64\sqrt{2}$ points were retained along each diagonal. The average number of points used from each projection was $N_R = 74$. Therefore, from Eq. (10), the approximate number of radial projections required in this case for fully sampled PR imaging is 116. By acquiring 110 projections with an FOV larger than the sample size, we have approximately satisfied the Nyquist criterion over the entire rat lung.

We anticipate that this work will set the stage for the challenge of accurately correlating local measurements of ^{3}He gas diffusion to histological measurements of lung architecture in animal disease models. The application of Eq. [4] to 3D imaging of a broad range of *b*-values may help distinguish subtle regional diffusion heterogeneities introduced by a disease state, such as emphysema. Although numerical simulations by Fichele et al. [42] suggest that the value R calculated by the Yablonskiy model may not be a sensitive indicator of mild emphysema, Yablonskiy et al. and Fichele et al. both agree that D_L should be sensitive to early emphysematous changes in the lung structure.

Acknowledgments

The authors gratefully acknowledge the animal preparation by A. Woodstock. The authors also thank B. Saam for supplying spin-exchange optical pumping cells. This work was funded by NIH NHLBI RO1 HL073598 and by Pacific Northwest National Laboratory's (PNNL's) Independent Research and Development (IR&D) program. Imaging was performed in the Environmental Molecular Sciences Laboratory (a national scientific user facility sponsored by the US Department of Energy's Office of Biological and Environmental Research), located at PNNL, which is operated for the DOE by Battelle.

Appendix

An alternative derivation of Eq. (8), which relates the apparent diffusional kurtosis to the diffusion anisotropy of the Yablonskiy model, utilizes the relationship obtained by Jensen et al. between the diffusional kurtosis and the variance of the diffusivity [23]:

$$K_{\mathrm{app}} = 3 \frac{\mathrm{var}(D)}{\overline{D}^2}. \tag{11}$$

Here, it is assumed that there are multiple non-interacting compartments with Gaussian diffusion in each compartment. From the random distribution of airway orientations assumed by Yablonskiy et al. [24],

$$D = D_L \cos^2\alpha + D_T \sin^2\alpha. \tag{12}$$

Thus, we can calculate:

$$\begin{aligned} \mathrm{var}(D) &= \int_0^{\pi} \frac{\sin\alpha}{2} (D_L \cos^2\alpha + D_T \sin^2\alpha - \overline{D})^2 \mathrm{d}\alpha \\ &= \frac{4}{45} D_{\mathrm{AN}}^2. \end{aligned} \tag{13}$$

By inserting the result of Eq. (13) into Eq. (11), the relationship of Eq. (8) is found.

References

[1] H.U. Kauczor, X.J. Chen, E.J.R. van Beek, W.G. Schreiber, Pulmonary ventilation imaged by magnetic resonance: at the doorstep of clinical application, Eur. Respir. J. 17 (2001) 1008–1023.

[2] J.C. Leawoods, D.A. Yablonskiy, B. Saam, D.S. Gierada, M.S. Conradi, Hyperpolarized He-3 gas production and MR imaging of the lung, Concept Magn. Reson. 13 (2001) 277–293.

[3] H.E. Möller, X.J. Chen, B. Saam, K.D. Hagspiel, G.A. Johnson, T.A. Altes, E.E. de Lange, H.U. Kauczor, MRI of the lungs using hyperpolarized noble gases, Magn. Reson. Med. 47 (2002) 1029–1051.

[4] X.J. Chen, H.E. Möller, M.S. Chawla, G.P. Cofer, B. Driehuys, L.W. Hedlund, G.A. Johnson, Spatially resolved measurements of

hyperpolarized gas properties in the lung in vivo. Part I: diffusion coefficient, Magn. Reson. Med. 42 (1999) 721–728.
[5] M.S. Conradi, D.A. Yablonskiy, J.C. Woods, D.S. Gierada, R.E. Jacob, Y.L.V. Chang, C.K. Choong, A.L. Sukstanskii, T. Tanoli, S.S. Lefrak, J.D. Cooper, He-3 diffusion MRI of the lung, Acad. Radiol. 12 (2005) 1406–1413.
[6] B.T. Saam, D.A. Yablonskiy, V.D. Kodibagkar, J.C. Leawoods, D.S. Gierada, J.D. Cooper, S.S. Lefrak, M.S. Conradi, MR imaging of diffusion of He-3 gas in healthy and diseased lungs, Magn. Reson. Med. 44 (2000) 174–179.
[7] R. Bammer, Basic principles of diffusion-weighted imaging, Eur. J. Radiol. 45 (2003) 169–184.
[8] G. Peces-Barba, J. Ruiz-Cabello, Y. Cremillieux, I. Rodriguez, D. Dupuich, V. Callot, M. Ortega, M.L.R. Arbo, M. Cortijo, N. Gonzalez-Mangado, Helium-3 MRI diffusion coefficient: correlation to morphometry in a model of mild emphysema, Eur. Respir. J. 22 (2003) 14–19.
[9] J.C. Woods, C.K. Choong, D.A. Yablonskiy, J. Bentley, J. Wong, J.A. Pierce, J.D. Cooper, P.T. Macklem, M.S. Conradi, J.C. Hogg, Hyperpolarized He-3 diffusion MRI and histology in pulmonary emphysema, Magn. Reson. Med. 56 (2006) 1293–1300.
[10] T.A. Altes, J. Mata, E.E. de Lange, J.R. Brookeman, J.P. Mugler, Assessment of lung development using hyperpolarized helium-3 diffusion MR imaging, J. Magn. Reson. Imaging 24 (2006) 1277–1283.
[11] C.L. Liu, R. Bammer, M.E. Moseley, Limitations of apparent diffusion coefficient-based models in characterizing non-Gaussian diffusion, Magn. Reson. Med. 54 (2005) 419–428.
[12] C.B. Wang, G.W. Miller, T.A. Altes, E.E. de Lange, G.D. Cates, J.P. Mugler, Time dependence of He-3 diffusion in the human lung: Measurement in the long-time regime using stimulated echoes, Magn. Reson. Med. 56 (2006) 296–309.
[13] J.C. Woods, D.A. Yablonskiy, K. Chino, T.S.K. Tanoli, J.D. Cooper, M.S. Conradi, Magnetization tagging decay to measure long-range He-3 diffusion in healthy and emphysematous canine lungs, Magn. Reson. Med. 51 (2004) 1002–1008.
[14] J. Stepisnik, Validity limits of Gaussian approximation in cumulant expansion for diffusion attenuation of spin echo, Physica B 270 (1999) 110–117.
[15] X.J. Chen, L.W. Hedlund, H.E. Moller, M.S. Chawla, R.R. Maronpot, G.A. Johnson, Detection of emphysema in rat lungs by using magnetic resonance measurements of He-3 diffusion, Proc. Natl. Acad. Sci. USA 97 (2000) 11478–11481.
[16] J.P. Dugas, J.R. Garbow, D.K. Kobayashi, M.S. Conradi, Hyperpolarized He-3 MRI of mouse lung, Magn. Reson. Med. 52 (2004) 1310–1317.
[17] J.F. Mata, T.A. Altes, J. Cai, K. Ruppert, W. Mitzner, K.D. Hagspiel, B. Patel, M. Salerno, J.R. Brookeman, E.E. de Lange, W.A. Tobias, H.T.J. Wang, G.D. Cates, J.P. Mugler, Evaluation of emphysema severity and progression in a rabbit model: comparison of hyperpolarized He-3 and Xe-129 diffusion MRI with lung morphometry, J. Appl. Physiol. 102 (2007) 1273–1280.
[18] J.C. LeaWoods, C.C. Choong, D.A. Yablonskiy, K. Chino, J.A. Pierce, J. Scheske, J.D. Cooper, M.S. Conradi, J. Hogg, Measuring changes in the severity of emphysema with hyperpolarized He-3 diffusion MRI, FASEB J. 18 (2004) A949.
[19] E.O. Stejskal, J.E. Tanner, Spin diffusion measurement: spin echoes in the presence of a time-dependent field gradient, J. Chem. Phys. 42 (1964) 288–292.
[20] D.C. Alexander, G.J. Barker, S.R. Arridge, Detection and modeling of non-Gaussian apparent diffusion coefficient profiles in human brain data, Magn. Reson. Med. 48 (2002) 331–340.
[21] V.G. Kiselev, K.A. Il'yasov, Is the "biexponential diffusion" bilexponential? Magn. Reson. Med. 57 (2007) 464–469.
[22] R. Trampel, J.H. Jensen, R.F. Lee, I. Kamenetskiy, G. McGuinness, G. Johnson, Diffusional kurtosis Imaging in the lung using hyperpolarized 3He, Magn. Reson. Med. 56 (2006) 733–737.
[23] J.H. Jensen, J.A. Helpern, A. Ramani, H.Z. Lu, K. Kaczynski, Diffusional kurtosis imaging: the quantification of non-Gaussian water diffusion by means of magnetic resonance imaging, Magn. Reson. Med. 53 (2005) 1432–1440.
[24] D.A. Yablonskiy, A.L. Sukstanskii, J.C. Leawoods, D.S. Gierada, G.L. Bretthorst, S.S. Lefrak, J.D. Cooper, M.S. Conradi, Quantitative in vivo assessment of lung microstructure at the alveolar level with hyperpolarized He-3 diffusion MRI, Proc. Natl. Acad. Sci. USA 99 (2002) 3111–3116.
[25] W.G. Johanson, A.K. Pierce, Lung structure and function with age in normal rats and rats with papain emphysema, J. Clin. Invest. 52 (1973) 2921–2927.
[26] R.E. Jacob, S.W. Morgan, B. Saam, He-3 spin exchange cells for magnetic resonance imaging, J. Appl. Phys. 92 (2002) 1588–1597.
[27] B. Chann, E. Babcock, L.W. Anderson, T.G. Walker, W.C. Chen, T.B. Smith, A.K. Thompson, T.R. Gentile, Production of highly polarized He-3 using spectrally narrowed diode laser array bars, J. Appl. Phys. 94 (2003) 6908–6914.
[28] T.G. Walker, W. Happer, Spin-exchange optical pumping of noble-gas nuclei, Rev. Mod. Phys. 69 (1997) 629–642.
[29] H.E. Möller, X.J. Chen, M.S. Chawla, B. Driehuys, L.W. Hedlund, G.A. Johnson, Signal dynamics in magnetic resonance imaging of the lung with hyperpolarized noble gases, J. Magn. Reson. 135 (1998) 133–143.
[30] B. Saam, W. Happer, H. Middleton, Nuclear-relaxation of He-3 in the presence of O-2, Phys. Rev. A 52 (1995) 862–865.
[31] L.W. Hedlund, G.P. Cofer, S.J. Owen, G.A. Johnson, MR-compatible ventilator for small animals: computer-controlled ventilation for proton and noble gas imaging, Magn. Reson. Imaging 18 (2000) 753–759.
[32] G. Krinke, The laboratory rat, the handbook of experimental animals, Academic Press, San Diego, CA, 2000, pp. 325.
[33] T. Lanz, J. Ruff, A. Weisser, A. Haase, Double tuned Na-23 H-1 nuclear magnetic resonance birdcage for application on mice in vivo, Rev. Sci. Instrum. 72 (2001) 2508–2510.
[34] J.M. Wild, M.N.J. Paley, L. Kasuboski, A. Swift, S. Fichele, N. Woodhouse, P.D. Griffiths, E.J.R. van Beek, Dynamic radial projection MRI of inhaled hyperpolarized He-3 gas, Magn. Reson. Med. 49 (2003) 991–997.
[35] D.C. Peters, F.R. Korosec, T.M. Grist, W.F. Block, J.E. Holden, K.K. Vigen, C.A. Mistretta, Undersampled projection reconstruction applied to MR angiography, Magn. Reson. Med. 43 (2000) 91–101.
[36] A.F. Gmitro, A.L. Alexander, Use of a projection reconstruction method to decrease motion sensitivity in diffusion-weighted MRI, Magn. Reson. Med. 29 (1993) 835–838.
[37] J.F. Kaiser, Digital filters, in: F.F. Kuo, J.F. Kaiser (Eds.), Systems Analysis by Digital Computer, Wiley, New York, NY, 1966.
[38] J.I. Jackson, C.H. Meyer, D.G. Nishimura, A. Macovski, Selection of a convolution function for fourier inversion using gridding, IEEE Trans. Med. Imaging 10 (1991) 473–478.
[39] D.A. Yablonskiy, G.L. Bretthorst, J.J.H. Ackerman, Statistical model for diffusion attenuated MR signal, Magn. Reson. Med. 50 (2003) 664–669.
[40] A.J. Swift, J.M. Wild, S. Fichele, N. Woodhouse, S. Fleming, J. Waterhouse, R.A. Lawson, M.N.J. Paley, E.J.R. Van Beek, Emphysematous changes and normal variation in smokers and COPD patients using diffusion He-3 MRI, Eur. J. Radiol. 54 (2005) 352–358.
[41] E.M. Haacke, R.W. Brown, M.R. Thompson, R. Venkatesan, Magnetic resonance imaging: physical principles and sequence design, J. Wiley & Sons, New York, 1999.
[42] S. Fichele, M.N.J. Paley, N. Woodhouse, P.D. Griffiths, E.J.R. van Beek, J.M. Wild, Finite-difference simulations of He-3 diffusion in 3D alveolar ducts: comparison with the "cylinder model, Magn. Reson. Med. 52 (2004) 917–920.